Published in the Proceedings of the 16th International Aluminum Alloys Conference (ICAA16) 2018
ISBN: 978-1-926872-41-4
by the Canadian Institute of Mining, Metallurgy & Petroleum

LONG TERM AGEING OF ALLOY 2618A

*C. Rockenhäuser[1], E. Augenstein[2], and B. Skrotzki[1]

[1]*Bundesanstalt für Materialforschung und -prüfung (BAM)*
Berlin, Germany
*(*Corresponding author: christian.rockenhaeuser@bam.de)*

[2]*Fraunhofer Institut für Werkstoffmechanik IWM*
Freiburg, Baden-Württemberg, Germany

ABSTRACT

The aluminium alloy 2618A is an Al-Cu-Mg alloy with additions of Fe and Ni, which is designed for long-term operation at elevated temperature in transportation and aerospace industries. The alloy degrades due to coarsening and dissolution of GPB zones and coarsening of S-Phase precipitates (Al_2CuMg). This work investigates the overageing process at the application relevant temperatures of 190 °C for durations ranging up to 25,000 h. The nm-sized precipitates were selectively imaged along the $<001>_\alpha$ direction of the Al matrix using dark-field transmission electron microscopy. The resulting images were then evaluated and allow the statistically relevant determination of radii distributions and the average radius of the precipitates dependent on temperature and heat treatment duration. Ostwald ripening of the S-phase does not describe the ageing process adequately. Instead, the evolution of GPB zones during the initial ageing regime needs to be considered in addition to the coarsening process of the S-phase. DSC measurements were performed to determine the presence of GPB zones in different ageing states. This will allow a quantitative description of the ageing process and a comparison to samples aged under external load.

KEYWORDS

Ageing, Coarsening, Dark-field transmission electron microscopy, Differential scanning calorimetry (DSC), Microstructure, S-Phase

INTRODUCTION

Alloy 2618A is an Al-Cu-Mg alloy, which is part of the 2XXX series of aluminium alloys. It is used in aerospace and transportation industry due to its desirable material properties for long term operation at elevated temperatures (Polmear, 2006). Fe and Ni are added to form intermetallic compounds, which retain microstructural stability at elevated temperatures (Bergsma, Li, & Kassner, 1996; Elgallad, Shen, Zhang, & Chen, 2014; Oguocha, Yannacopoulos, & Jin, 1996; Wang & Yi, 2006). The size and distribution of the nm-sized S-phase formed from the supersaturated solid solution (SSSS) during heat treatments mainly controls the strength (Khan, Starink, & Yan, 2008; Liu, Zhang, Ding, Sun, & Chen, 2003; Parel, Wang, & Starink, 2010; Shih, Ho, & Huang, 1996; Wang, Starink, & Gao, 2006). The S-phase has the composition Al_2CuMg and is orthorhombic under equilibrium conditions (Heying, Hoffmann, & Pottgen, 2005; Perlitz & Westgren, 1943). Early experiments proposed the following decomposition of the S-phase sequence during heat treatments (Hardy & Heal, 1954; Silcock, 1961):

$$\text{SSSS} \rightarrow \text{GPB zone} \rightarrow \text{S''+S'} \rightarrow \text{S'+S} \rightarrow \text{S}$$

The Guinier-Preston-Bagaryatsky (GPB) zones are rod-shaped predecessors of the S-phase with a diameter of 1-2 nm and the S'' and S' precipitates were reported to be metastable variants of the S-phase. However, the decomposition sequence of the hardening phases during isothermal ageing remains under debate (Styles, Hutchinson, Chen, Deschamps, & Bastow, 2012; Styles et al., 2015). In addition, external loads may influence the precipitation of the hardening phases in aluminium alloys strongly (Bai et al., 2015; Chen, Chen, Guo, & Deng, 2016; Liu et al., 2014; Skrotzki, Shiflet, & Starke, 1996). Recently, the authors provided experimental evidence (Rockenhäuser, Schriever, Hartrott, Piesker, & Skrotzki, 2018), that the long-term coarsening process in alloy 2618A under loading conditions can be described by the following coarsening law:

$$r^5 - r_0^5 = k(t - t_0) \tag{1}$$

Here, r is the mean radius, r_0 the mean initial radius, t the coarsening time, t_0 the initial time, and k a constant. The coarsening law according to equation (1) can be derived similar to the regular Ostwald ripening and was proposed by Ardell (Ardell, 1972). Ardell assumes that the precipitates are connected by a dislocation network and the mass transport elapses with increased speed (compared to Ostwald ripening) along dislocations as diffusion pathways. This is a reasonable assumption in case of creep samples. However, the study was not able to describe the coarsening process without external load satisfactory. Neither an Ostwald ripening process, which is described by the following equation,

$$r^3 - r_0^3 = k(t - t_0) \tag{2}$$

nor Ardells model conformed to the increase of the average radius of the unstressed samples. The authors suggest that this is due to the presence of GPB zones in the initial T61 state of the alloy, which influences the ageing process of the S-phase precipitates. The present paper further investigates the ageing process of unstressed samples and shows first result regarding the presence of GPB zones during ageing. The quantitative description of the ageing process can then be used for lifetime models based on material simulation software (e. g. MatCalC).

EXPERIMENTAL DETAILS

All fabricated and investigated samples are prepared from forged circular blanks made from alloy 2618A in a T61 condition according to DIN EN 515 (DIN EN 515, 2017) with a chemical composition corresponding to DIN EN 573 (DIN EN 573-3, 2013). The T61 condition is a slightly underaged condition

resulting from a solution heat treatment (530 °C, 8 h) and an additional ageing treatment (195 °C, 28 h). Square bulk samples (3 cm x 3 cm, thickness 4 mm) were cut by wire-cut electrical discharge machining from the blank for conventional ageing. The resulting cuboids were aged at 190 °C for 250 h, 2,500 h, 5,000 h, and 25,000 h). The temperature accuracy of the heat treatments is ± 2 °C.

The samples were conventionally prepared for transmission electron microscopy (TEM) after ageing. Platelets with a thickness of about 500 µm were mechanically cut from the aged samples. Then the samples were ground using increasingly fine abrasive papers to a final thickness of about 130 µm. The final step of mechanical preparation was punching uniform discs with a diameter of 3 mm. The discs were electropolished using a twin-jet Tenupol-3 electropolishing device (Struers) at a voltage of 12 V to achieve electron transparency. An electrolyte with two parts methanol (pure) and one part nitric acid (65 %) cooled to -20 °C was used. The electron microscopical investigations were performed in a JEM-2200FS TEM/Scanning TEM with a field-emission gun operating at 200 kV. At least 10 images were taken at different places of each sample and at least 300 precipitates were evaluated for each presented radii distribution.

The samples for differential scanning calorimetry (DSC) were prepared from the forged blank and an aged square bulk sample by wire-cut electrical discharge machining. The resulting cylinders with a diameter of 5 mm and a height of about 0.5 mm were then investigated in a DSC 404C Pegasus differential scanning calorimeter. The samples were heated from room temperature to 550 °C using a heating rate of 10 K/min and the corrected heat flow was extracted from the experimental data. All calibration procedures (temperature measurement, environmental influences, heat flow sensitivity) were performed according to DIN 51007 (DIN 51007, 1994).

RESULTS

To systematically investigate the Al_2CuMg precipitate radii, dark-field TEM (DFTEM) was performed for all investigated samples. This allows selective imaging of the S-Phase precipitates and GPB zones. The S-phase precipitates form as rods along the $<001>_\alpha$ direction of the α-Al matrix. The GPB zones as predecessors of the S-phase are also oriented along this direction. Therefore, the samples were oriented in the $[001]_\alpha$ direction for the DFTEM investigations. The rod shaped precipitates cause streaks in between the matrix reflections and an aperture was used to select the streaks for imaging (Wang & Starink, 2005). The insertion of the aperture also excludes contrast contributions of the primary phases present in the samples (Al_9FeNi, Mg_2Si). Representative dark-field images of the Al_2CuMg precipitates are shown in Figure 1a-e). The contrast of all presented DFTEM images was (linearly) enhanced for better visibility. The spots with bright contrast correspond to S-phase precipitates and GPB zones oriented along the $[001]_\alpha$ direction and penetrate the image plane. The elongated lath shaped contrasts are caused by rods oriented orthogonal to the incident electron beam. The rods are imaged along the $[001]_\alpha$, $[010]_\alpha$ and $[100]_\alpha$ directions of the Al matrix. Rods aligned along the $[001]_\alpha$ direction (i.e. with their rod axis orthogonal to the image plane) produce more contrast in comparison to the rods orientated orthogonal to the incident beam direction $[001]_\alpha$ (i.e. with their rod axis parallel to the image plane), since the electron beam passes the former by their full length. The latter are only passed by the electron beam across their diameter and thus produce less contrast. The bright contrast spots in Figure 1a) correspond to the precipitates of the initial T61 state. Smaller and larger S-phase precipitates are clearly visible. The smaller S-phase precipitates cannot be distinguished from the GPB zones. Coarsening of the initially smaller particles occurs during isothermal heat treatments at 190 °C for 250 h, 2,500 h, 5,000 h, and 25,000 h. The resulting larger bright contrasts can be seen in Figure 1b-e). All precipitates imaged by DFTEM were in the following analysis considered as cylindrical rods with radius r and length l. It was not possible to quantify the length of the precipitates using DFTEM imaging due to the low contrast of the rods parallel to the image plane. Therefore, the quantitative analysis focused on the precipitate radius.

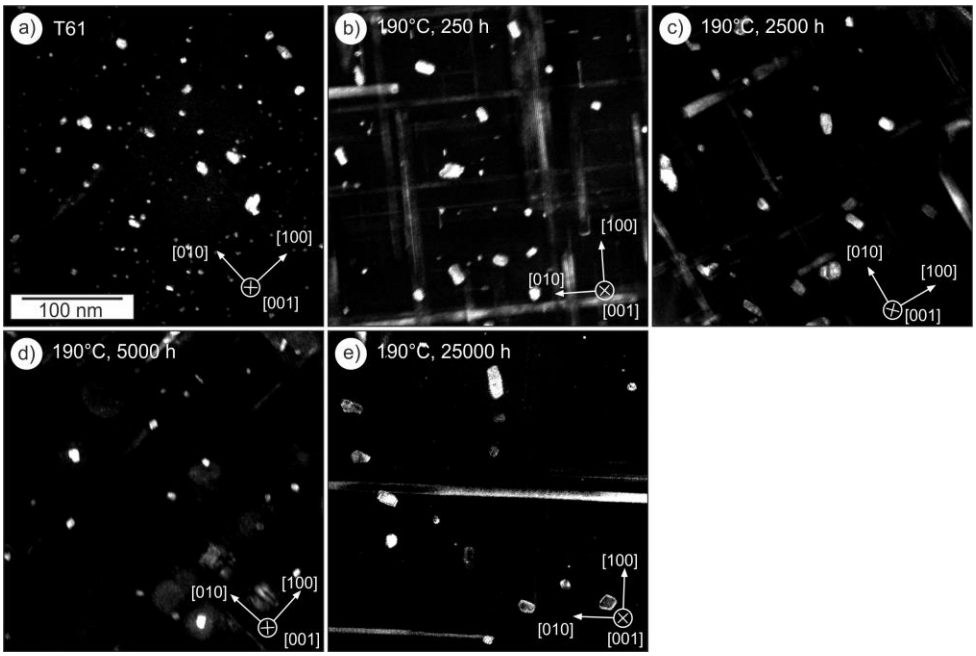

Figure 1. Dark-field images of the Al_2CuMg precipitates oriented along the [001] zone axis of the Al-matrix for a) T61, b) 190 °C, 250 h, c) 190 °C, 2,500 h, d) 190 °C, 5,000 h, and d) 190 °C, 25,000 h

The Al_2CuMg precipitates from multiple images of each sample were evaluated and then used to generate cumulative radii distributions normalized to the total number of precipitates for each sample. The method to obtain the distribution is described in more detail in a previous publication (Rockenhäuser et al., 2018). A log-normal distribution (Du, Holmedal, Friis, & Marioara, 2016)

$$n(r) = \frac{1}{2\sqrt{2\pi} r \sigma_{geo}} exp\left(\frac{\left(ln\left(\frac{r}{r_m}\right)\right)^2}{2\sigma_{geo}} \right) \quad (3)$$

with the particle radius, r, the median particle radius, r_m, and the geometric standard deviation, σ, was used to fit the measured radii distributions. The comparison of the experimental data and the fitted functions according to equation (3) are shown in Figure 2a-e). The bars correspond to the experimentally determined number of particles in the investigated samples and are normalized to the total number of precipitates found for the respective state. The number of particles for each state was at least 300 from at least two different samples with at least 10 evaluated images. The fitted log-normal distributions are plotted as a line in the graphs and show good agreement with the experimental data. The fits for all distributions converged.

The radii distributions of the initial state and the isothermally aged samples are shown in Figure 2a-e). The radii distributions in Figure 2a-e) indicate that with increasing average precipitate radius the initially narrow distribution of the initial state broadens with increasing duration and the distribution maximum moves to higher radii (Figure 2b-e)). Note the different scales (y-axis) in Figure 2a) and b) in comparison to Figure 2 c-e).

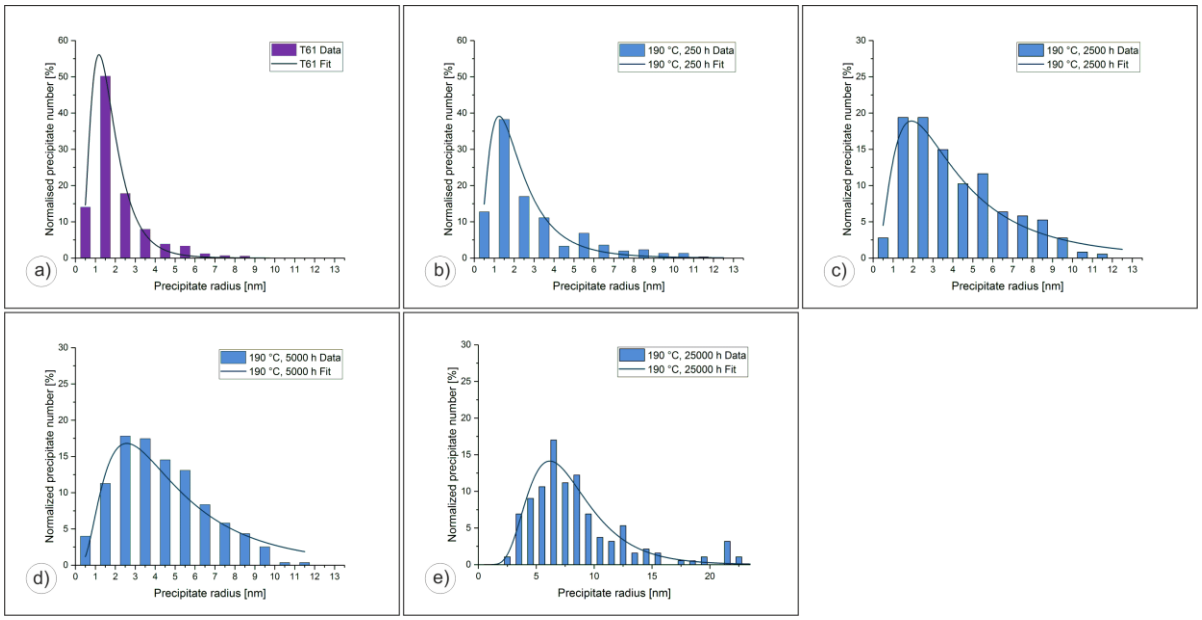

Figure 2. Fits of radii distributions including data of samples with the following heat treatments a) initial state (T61), b) 190 °C, 250 h, c) 190 °C, 2,500 h, d) 190 °C, 5,000 h, d) 190 °C, 25,000 h

r_m and σ were determined from the raw data for all samples. In case of a lognormal distribution, the average radius is not identical to the median radius and can be calculated from r_m and σ by the following equation (Aitchison & Brown, 1957):

$$r_a = r_m exp\left(\frac{\sigma_{geo}^2}{2}\right) \tag{4}$$

The results of the DSC measurements are shown in Figure 4. There are several features in the graph of the initial state (T61). An endothermic peak, A, between 230 C and 270 °C is followed by an exothermic peak, B, between 270 °C and 330 °C. Then a broad endothermic effect, C, in the temperature range between 340 °C and 470 °C follows. The measurement concludes with a sharp exothermic peak D between 470 °C and 550 °C. The sample heat treated at 190 °C for 8,760 h exhibits less features. Only the broad endothermic effect, C, and the sharp exothermic peak at a slightly lower temperature (460 °C to 540 °C) were observed.

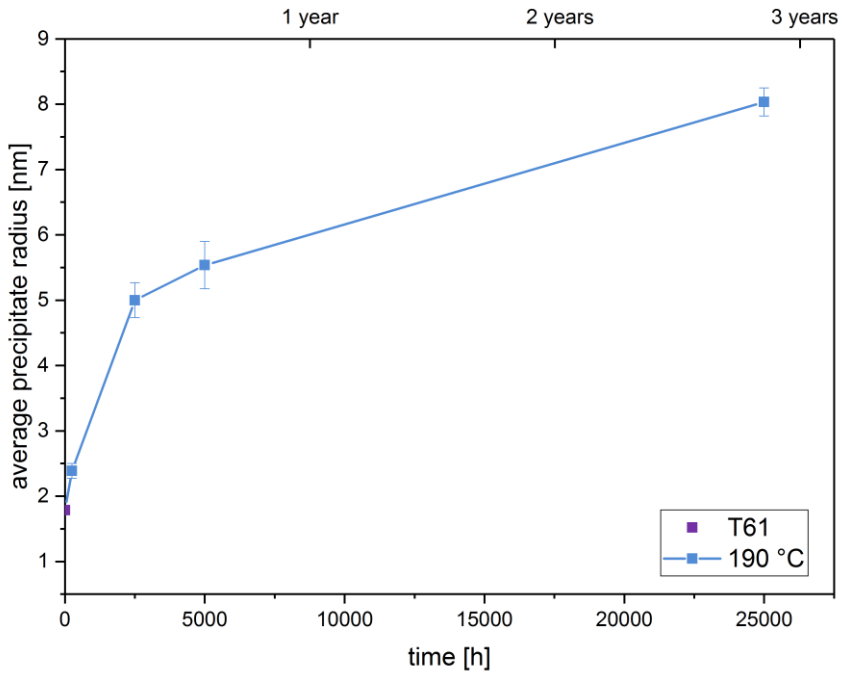

Figure 3. Average precipitate radius r_a vs. ageing time. The blue line connects the initial T61 state with the aged samples and is only a guide to the eye.

The development of the average particle radii calculated using equation (4) vs. time is shown in Figure 3 for isothermal ageing. It shows that the average radii increase during ageing. The errors include the statistical error and the systematic error of the size measurement in the electron microscopical images. The average radius increases from 1.79 nm in the T61 state to 8.03 nm after 25,000 h. Note that the increase is more pronounced in the beginning.

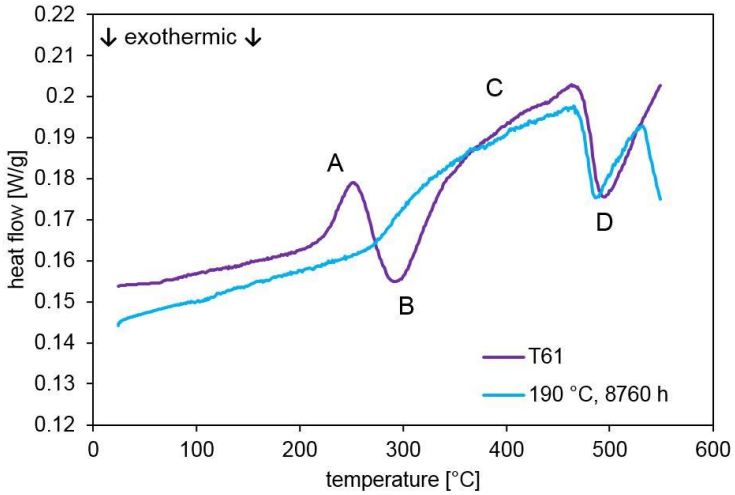

Figure 4. Results of the DSC measurements of the initial state T61 and a sample aged at 190 C for 8,760 h.

DISCUSSION

The average precipitate radii shown in Figure 3 clearly show that the GPB zones and S-phase precipitates present in the alloy coarsen during ageing. However, neither an Ostwald ripening process (equation (2)) nor Ardell's model (equation (1)) result in an acceptable fit for the acquired data. It is problematic that both coarsening models only consider the ripening of one secondary phase. In this case there are two different kinds of structures present in the initial state (T61). This means that interpretation of the radii distributions, which does not discriminate between GPB zones and S-phase leads to difficulties. A system with only one secondary phase would allow a direct comparison to the two models. It is known from previous studies that the GPB zones eventually dissolve during the coarsening process. To investigate only the S-phase, it is required to know when the GPB zones are completely dissolved. This would then define the starting point of the ripening process of the S-phase.

DSC measurements allow discerning, if the different ageing states still contain GPB zones or if they were completely dissolved. Two preliminary measurements were performed and can be compared to a study using a similar S-phase containing material which allows a cautious interpretation of the DSC measurements (Wang & Starink, 2007). They found an exothermic effect between 230 °C and 340 °C, which is attributed to the formation of the S-phase. This coincides well to the measured exothermic peak B between 270 °C and 330 °C for the initial state T61. They also find that the S-phase formation peak is preceded by an endothermic effect between 160 °C and 240 °C, which corresponds to the dissolution of GPB zones. Here the endothermic peak (A) is also present for the initial state T61 and suggests the dissolution of the GPB zones. However, it is found at slightly higher temperatures between 230 C and 270 °C. A broad endothermic effect was found for both samples between about 340 °C and 470 °C. The corresponding part of curve in the study of Wang & Starink also shows this effect between 340 °C and 500 °C and implicates the dissolution of the S-phase. In the present study this means that for the initial state the dissolution of the GPB zone (A), formation of the S-phase (B), and the subsequent dissolution of the S-phase (C) is observed. In contrast, only the dissolution of the S-phase was found for the sample aged at 190 °C for 8,760 h. This means that subsequent DSC measurements enable to identify the ageing state, where no GBP zones are left. The then following coarsening process should elapse as an Ostwald ripening after that point in time.

CONCLUSIONS

The ageing process of alloy 2618A was investigated for isothermally aged samples at 190 °C. Radii distributions were determined for the S-phase, which is responsible for desirable material properties, using DFTEM. The images clearly indicate that coarsening of the S-phase occurs during ageing. It was possible to calculate average precipitate radii using the acquired distributions. However, no applicable coarsening law was found for the ageing process of the GPB zones and the S-phase. This is attributed to the simultaneous presence of the two secondary phases. To find a viable coarsening law, the investigation of only one secondary phase is necessary. DSC measurements were performed to pinpoint the ageing time, where no GPB zones are left. It was shown by preliminary DSC investigations that the technique is suitable to determine this point in time during the ageing process. The presented data can be used for simulations of the microstructure evolution to integrate the microstructure into component lifetime models.

ACKNOWLEDGMENTS

The authors express their thanks to the Research Association for Combustion Engines (FVV, Frankfurt) for the selection of this research project as well as to the German Federal Ministry of Economic Affairs and Energy (BMWi) and the German Federation of Industrial Research Associations (AiF) for funding (IGF-No. 17734).

REFERENCES

Aitchison, J., & Brown, J. A. C. (1957). *The lognormal distribution with special reference to its uses in economics*. Cambridge: Cambridge University Press.

Ardell, A. J. (1972). Coarsening of grain-boundary precipitates. *Acta Metallurgica, 20*(4), 601-609. https://doi.org/10.1016/0001-6160(72)90015-6

Bai, S., Zhou, X., Liu, Z., Ying, P., Liu, M., & Zeng, S. (2015). Atom probe tomography study of Mg-dependent precipitation of Ω phase in initial aged Al-Cu–Mg–Ag alloys. *Materials Science and Engineering: A, 637*(0), 183-188. https://doi.org/10.1016/j.msea.2015.04.052

Bergsma, S. C., Li, X., & Kassner, M. E. (1996). Effects of thermal processing and copper additions on the mechanical properties of aluminum alloy ingot AA 2618. *Journal of Materials Engineering and Performance, 5*(1), 100-102. https://doi.org/10.1007/bf02647276

Chen, J. Q., Chen, Z. G., Guo, X. B., & Deng, Y. L. (2016). Changing distribution and geometry of S' in Al-Cu-Mg single crystals during stress aging by controlling the loading orientation. *Materials Science and Engineering: A, 650*, 154-160. https://doi.org/10.1016/j.msea.2015.09.120

DIN 51007:1994-6: Thermal analysis; differential thermal analysis; principles, (1994).

DIN EN 515:2017-05: Aluminium and aluminium alloys - Wrought products - Temper designations, (2017).

DIN EN 573-3: Aluminium and Aluminium alloys - chemical composition and form of wrought products - part 3: Chemical composition and form of products, (2013).

Du, Q., Holmedal, B., Friis, J., & Marioara, C. D. (2016). Precipitation of Non-spherical Particles in Aluminum Alloys Part II: Numerical Simulation and Experimental Characterization During Aging Treatment of an Al-Mg-Si Alloy. *Metallurgical and Materials Transactions A, 47*(1), 589-599. https://doi.org/10.1007/s11661-015-3196-6

Elgallad, E. M., Shen, P., Zhang, Z., & Chen, X. G. (2014). Effects of heat treatment on the microstructure and mechanical properties of AA2618 DC cast alloy. *Materials & Design, 61*(0), 133-140. https://doi.org/10.1016/j.matdes.2014.04.045

Hardy, H. K., & Heal, T. J. (1954). Report on precipitation. *Progress in Metal Physics, 5*, 143-278. https://doi.org/10.1016/0502-8205(54)90006-4

Heying, B., Hoffmann, R. D., & Pottgen, R. (2005). Structure refinement of the S-phase precipitate $MgCuAl_2$. *Zeitschrift Fur Naturforschung Section B-a Journal of Chemical Sciences, 60*(5), 491-494.

Khan, I. N., Starink, M. J., & Yan, J. L. (2008). A model for precipitation kinetics and strengthening in Al–Cu–Mg alloys. *Materials Science and Engineering: A, 472*(1–2), 66-74. https://doi.org/10.1016/j.msea.2007.03.033

Liu, G., Zhang, G. J., Ding, X. D., Sun, J., & Chen, K. H. (2003). Modeling the strengthening response to aging process of heat-treatable aluminum alloys containing plate/disc- or rod/needle-shaped precipitates. *Materials Science and Engineering: A, 344*(1-2), 113-124. https://doi.org/10.1016/s0921-5093(02)00398-2

Liu, X. Y., Pan, Q. L., Zhang, X. L., Liang, S. X., Gao, F., Zheng, L. Y., & Li, M. X. (2014). Creep behavior and microstructural evolution of deformed Al–Cu–Mg–Ag heat resistant alloy. *Materials Science and Engineering: A, 599*(0), 160-165. https://doi.org/10.1016/j.msea.2014.01.090

Oguocha, I. N. A., Yannacopoulos, S., & Jin, Y. (1996). The structure of Al_xFeNi phase in Al-Cu-Mg-Fe-Ni alloy (AA2618). *Journal of Materials Science, 31*(21), 5615-5621. https://doi.org/10.1007/bf01160806

Parel, T. S., Wang, S. C., & Starink, M. J. (2010). Hardening of an Al-Cu-Mg alloy containing Types I and II S phase precipitates. *Materials & Design, 31*, S2-S5. https://doi.org/10.1016/j.matdes.2009.12.048

Perlitz, H., & Westgren, A. (1943). The crystal structure of Al_2CuMg. *Ark. Kem. Mineral. Geol, 16*, 1-5.

Polmear, I. J. (2006). *Light Alloys* (4th. ed.). Burlington, MA, USA: Butterworth-Heinemann.

Rockenhäuser, C., Schriever, S., Hartrott, P. v., Piesker, B., & Skrotzki, B. (2018). Comparison of long-term radii evolution of the S-phase in aluminum alloy 2618A during ageing and creep. *Materials Science and Engineering A*.

Shih, H. C., Ho, N. J., & Huang, J. C. (1996). Precipitation behaviors in Al-Cu-Mg and 2024 aluminum alloys. *Metallurgical and Materials Transactions A-Physical Metallurgy and Materials Science, 27*(9), 2479-2494. https://doi.org/10.1007/bf02652342

Silcock, J. M. (1961). The structural ageing characteristics of Al-Cu-Mg Alloys with Copper-Magnesium weight ratios of 7-1 and 2.2-1. *Journal of the Institute of Metals, 89*(6), 203-210.

Skrotzki, B., Shiflet, G. J., & Starke, E. A. (1996). On the effect of stress on nucleation and growth of precipitates in an Al-Cu-Mg-Ag alloy. *Metallurgical and Materials Transactions A-Physical Metallurgy and Materials Science, 27*(11), 3431-3444. https://doi.org/10.1007/bf02595436

Styles, M. J., Hutchinson, C. R., Chen, Y., Deschamps, A., & Bastow, T. J. (2012). The coexistence of two S (Al_2CuMg) phases in Al–Cu–Mg alloys. *Acta Materialia, 60*(20), 6940-6951. https://doi.org/10.1016/j.actamat.2012.08.044

Styles, M. J., Marceau, R. K. W., Bastow, T. J., Brand, H. E. A., Gibson, M. A., & Hutchinson, C. R. (2015). The competition between metastable and equilibrium S (Al_2CuMg) phase during the decomposition of AlCuMg alloys. *Acta Materialia, 98*, 64-80. https://doi.org/10.1016/j.actamat.2015.07.011

Wang, J. H., & Yi, D. Q. (2006). Preparation and properties of alloy 2618 reinforced by submicron AlN particles. *Journal of Materials Engineering and Performance, 15*(5), 596-600. https://doi.org/10.1361/105994906x136133

Wang, S. C., & Starink, M. J. (2005). Precipitates and intermetallic phases in precipitation hardening (Al-Cu-Mg-(Li) based alloys. *International Materials Reviews, 50*(4), 193-215.

Wang, S. C., & Starink, M. J. (2007). Two types of S phase precipitates in Al-Cu-Mg alloys. *Acta Materialia, 55*(3), 933-941. https://doi.org/10.1016/j.actamat.2006.09.015

Wang, S. C., Starink, M. J., & Gao, N. (2006). Precipitation hardening in Al-Cu-Mg alloys revisited. *Scripta Materialia, 54*(2), 287-291. https://doi.org/10.1016/j.scriptamat.2005.09.010